Mapping tidal currents at a shallow tidal channel junction using the fluvial acoustic tomography system

C. Xiao [1], K. Kawanisi [1*], R. Torigoe [1], M. B. Al Sawaf [1]

[1] Department of Civil and Environmental Engineering, Graduate school of Engineering, Hiroshima University, Higashihiroshima, Japan

*Corresponding author.

E-mail address: kiyosi@hiroshima-u.ac.jp (K. Kawanisi)

Key points:

- Continuous 2D tidal currents were reconstructed by inverse method using 14 acoustic paths with six fluvial acoustic tomography (FAT) systems
- 2D tidal currents inversed by FAT with short intervals during a period of ~34.4 days at a shallow tidal junction
- Nonstationary river-tide dynamics at a shallow tidal junction were discussed based on the inversed tidal currents

Abstract

For the first time, we monitored continuous 2D tidal currents at a shallow tidal junction using the fluvial acoustic tomography (FAT) system during a period of ~ 34.4 days. The horizontal distribution and spatiotemporal variation of the tidal velocities were efficiently estimated by the inverse analysis method, and the reconstructed velocity patterns agreed well with the recorded acoustic Doppler current profiler series data. Additionally, the high frequency observation interval (1-min) used provided us with the opportunity to detect the rapid processes of the transformation of tidal current patterns during flood tide at the junction. These results further demonstrate that FAT is a potent tool for continuously mapping variable 2D tidal currents at shallow tidal junctions. Furthermore, tidal harmonic analyses of the reconstructed tidal currents were performed to clarify the nonlinear spatial evolution processes of the variations in tidal energy, when tides propagated from the estuary to the tidal junction. The sub-tide species (*Mm*, *MSf*) caused significant fortnightly variations in the tidal range along the tidal branches. The variations in the tidal current were dominated by semidiurnal species (D2: M_2, S_2, N_2, L_2), followed by diurnal species (D1: K_1, O_1, Q_1) and quarter-diurnal species (D4: M_4, MS_4). The M_4/M_2 amplitude ratios were higher during low river discharge periods, signifying that the nonlinear M_4 tidal distortion varies with river discharge. River-tide interactions strongly affected tidal asymmetry. It is believed that this study provides further understanding of hydrological research in shallow tidal systems.

1. Introduction

Ocean acoustic tomography (OAT) was suggested as a potent oceanographic technique to investigate mesoscale oceanic phenomena (Munk et al., 1995). Furthermore, to extend the applications of OAT in coastal areas for the continuous monitoring of tidal currents, coastal acoustic tomography (CAT) was designed since the 1990s (Kaneko et al., 1994; Yamaguchi et al., 2005; Yamoaka et al., 2002). The fluvial acoustic tomography (FAT) system is a promoted generation can be utilized in quite shallow waters to investigate shallow currents, in riverine and tidal environments ranging from ~0.5 m up to 10 m depth (Kawanisi et al., 2010).

Some studies have already presented some applications using only two crossing paths to reconstruct velocity magnitude and direction; for example, the dam flush in a mountainous river was observed (Kawanisi et al., 2013) and the tidal flow in a shallow tidal channel was measured (Razaz et al., 2013). Furthermore, (Razaz et al. (2015); 2016) positioned eight FATs in a shallow mountainous river and tidal channel to map depth-averaged current distributions. In the case of a mountainous river, although the boundary is meandering, there are no saltwater-wedge intrusion effects on sound propagation patterns. In the case of a tidal channel, salt-wedge intrusion effects occur and should be carefully considered. A continuous measurement of 2D tidal current fields at a shallow tidal junction with FAT to consider boundary and saltwater intrusion effects has not been conducted. A previous study (Danial et al., 2019) at a tidal junction using FAT only utilized two crossing paths to discuss tidal discharge and phase difference.

The exploration of river-tide dynamics at tidal junctions, associated with the interactions between river flow, tidal waves, and the bathymetry/geometrical shape of tidal branches, have been scarcely studied (Danial et al., 2019). In tidally influenced rivers, the intrusion of tides onto tidal junctions significantly complicates the processes of flow division (Sassi et al., 2012). Dinehart and Burau (2005) observed current variations at the tidal junction of the Sacramento River, which exhibited highly asymmetrical patterns during ebb and flood. In tidally influenced estuaries, tidal asymmetry and tide-induced residual circulations could generate a significant influence on the distribution of currents over distributary channel networks. Additionally, tidal propagation is strongly affected by river discharge in tidally influenced rivers and vice versa (Lu et al., 2015). Owing to the effects of bottom friction and river discharge, tidal waves propagating from the river mouth to upstream areas become distorted and damped (Sassi & Hoitink, 2013). Previous studies only focused on the results of subtidal water level structures for streamflow regimes in tidal rivers, and most of the studies were based on numerical models (Cai et al., 2018; Guo et al., 2014) or short/long time-series data, such as river discharges and water levels recorded at several gauging stations (Guo et al., 2015). To the best of our knowledge, detailed investigations on river-tide dynamics based on continuous 2D tidal current data inversed by FAT have never been conducted.

In this study, we performed an experiment over one month with six FAT systems at a shallow tidal junction, Hiroshima, Japan, in 2020. This study aims to characterize the tidal regime in terms of a continuous 2D tidal current field, tidal asymmetry, tidal dampening, the evolution of tidal constituents, and the propagation of tides at the shallow tidal junction using FAT inversed results. We intend to collect several pieces of evidence to demonstrate the response process of river-tide dynamics at the tidal junction. The rest of this paper is structured as follows. Introductions of the study area and methods are prepared in Section 2. Section 3 presents the inverse results at the junction. Section 4 further discusses the tidal regime and river-tide interactions at the junction based on the tidal currents reconstructed by the FAT. Finally, Section 5 presents the main conclusions in this study.

2. Study area and methods

2.1 Study area

The Ota River system is a network with several tide-dominated channels that flows through Hiroshima City, west of Japan. As shown in Figure 1a, the Ota River bifurcates around 9 km upstream from the river mouth into two major branches. The runoff in the Otagawa floodway are controlled by rows of Gion sluice gates, whereas the Oshiba sluice gates are always open throughout the year (Figure 1a). In this work, the studied tidal junction is situated in the mid-reach of the Ota River network, almost 2.5 km downstream from the Oshiba gates and almost 5.8 km upstream from the river mouth, which is under the influence of saltwater intrusion and the freshwater discharge flowing from upriver areas. Salt-wedge intrusion in the Ota River can reach areas up to 11.5 km upstream from the river mouth (Danial et al., 2019).

The shallow tidal junction involves three branches (Figure 1c): i) upstream (Kyu Ota River) is the northern branch, ii) downstream (Kyu Ota River) is the eastern branch, and iii) the Tenma River is the western branch. Danial et al. (2019) reported that the downstream (Kyu Ota River) is deeper and wider than the Tenma River. Riverbed levels for the eastern and western branches were approximately -3 T.P. m and -2 T.P. m, respectively. The northern branch is wider than both the eastern and western branches, and the riverbed level varies from -2.5 T.P. m to -3.0 T.P. m. In general, due to the frequent intrusion of saline water, freshwater discharge, and irregular bathymetry (Danial et al., 2019), the surveyed area is characterized by unsteady and complex flow distributions.

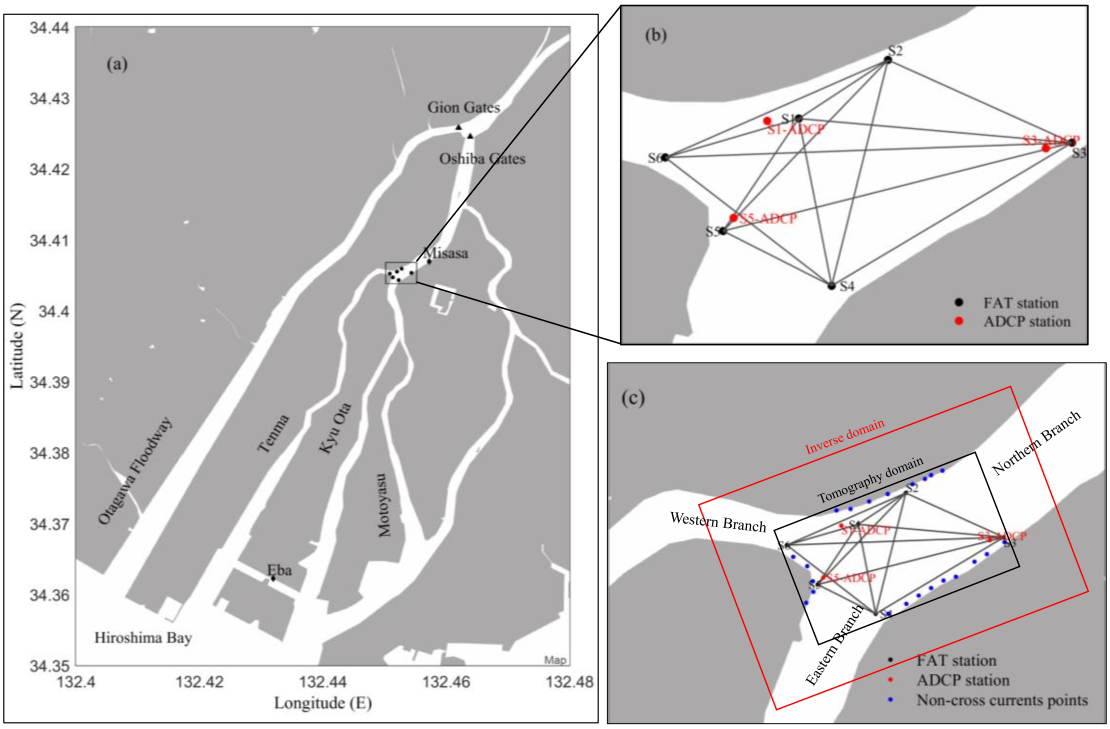

Figure 1. Diagrams for the experimental area: The locations of the FAT stations (S1 to S6) and fixed ADCP stations are showed by black and red dots, respectively. Acoustica paths among the FAT stations are denoted by solid black lines.

2.2 Instruments and Methods

The FAT observation was carried out for ~ 34.4 days (February 21– March 26, 2020), which covered two fortnightly tidal cycles (spring/neap cycle). As shown in

Figure 1b, six acoustic FAT transducers were placed along the riverbanks in an area almost 310 m length and 170 m width (Figure 1c). Simultaneous reciprocal transmissions were conducted along 14 transmission lines. During the observation period, acoustic signals with a 30-kHz central frequency were transmitted simultaneously from each source and then received by the other stations every minute. The transmitted sound was modulated by a M-sequence with the 9th order, increasing the processing gain by approximately 27.1 dB. The successful percentages of sound transmission data along 14 rays varied from 19% to 92% (Figure 2b). Missing data during the observation period were mainly triggered by the irregular, shallow region. Owing to the multiple reflections from the water surface and riverbed, the rays could not arrive at the receivers because of large transmission losses. The travel time difference series data were smoothed by a 1-h low-pass filter approach to erase the effects of the high-frequency noise, and, subsequently, be utilized in the inverse problem to estimate the 2D tidal current fields. The root mean squares error (RMSE) between the 1-min original and 1-h low-pass filtered travel time difference data fluctuated between 0.01 and 0.1 ms for the entire recorded data. The RMSE values caused errors in velocity that ranged from 0.06 to 0.21 m/s for all the station pairs, with a determined sound speed of 1475 m/s and constant station-to-station lengths.

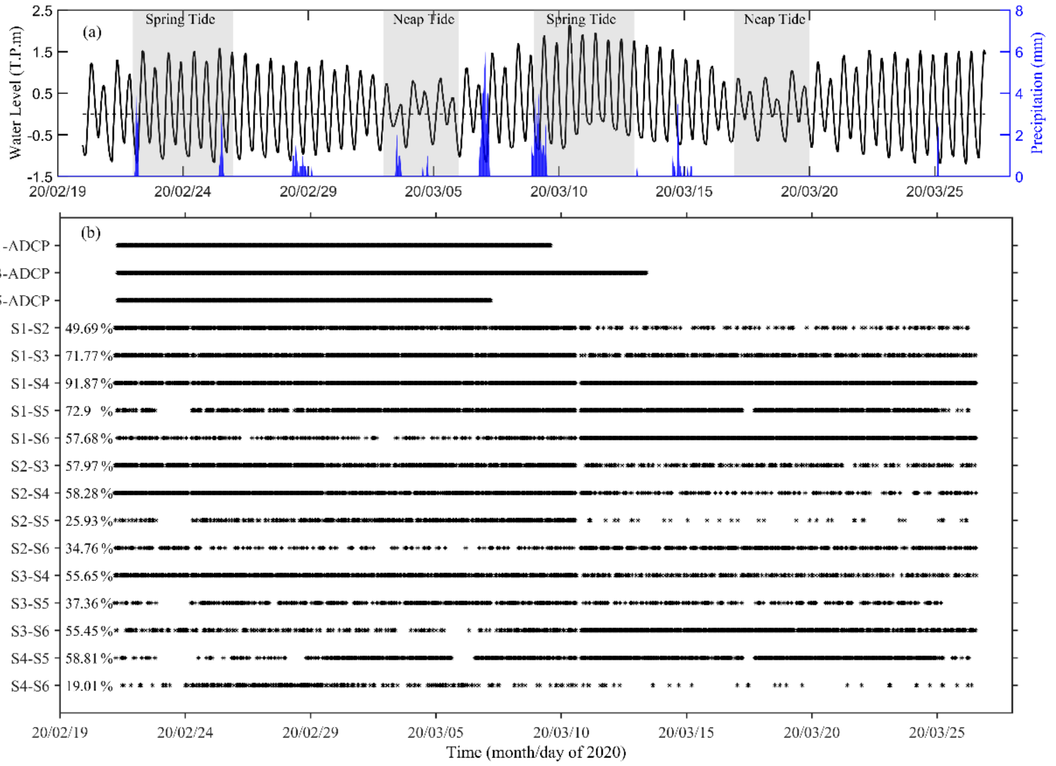

Figure 2. Synchronized FAT and ADCP measurements: (a) water level data was monitored at the Misasa gauging station, and precipitation data were acquired from the Japan Meteorological Agency, (b) observation periods of the fixed ADCP and time schedules of the successful percentages of reciprocal sound transmission between each settled station pair.

As shown in Figure 1b, three 2 MHz ADCPs (Aquadopp Profiler, Nortek) were placed to observe the 3D velocity variations in the water column, with a 60-second average interval and a 2-min sampling interval close to stations S1 and S3, and a 5-min sampling interval close to station S5. The bin size and blank distance were both set to 0.1 m. The bin number was 50. Owing to the difference in battery life and the capacity of each ADCP, observations close to stations S1, S3, and S5 were performed from February 21 to March 9, February 21 to March 13, and February 21 to March 7, respectively. Along with the FAT measurements, several routes of Teledyne RDI StreamPro ADCP were performed along four transects (S1-S3, S1-S6, S3-S5, S4-S5) to provide reference velocity data on March 6, 2020. All data were referenced to bottom tracking. Each transect started from and stopped near the riverbank.

Because FAT primarily observes the sound travel time between the settled acoustic stations. Relying on the travel time differences of the acoustical station pairs, the horizontal distributions of the depth-averaged velocity can be effectively mapped by the inverse analysis. The inverse method has been employed by different researchers (Razaz et al., 2015; Yamaguchi et al., 2005; Yamoaka et al., 2002; Zhang et al., 2017; Zhu et al., 2015). In this work, we followed the basic formulas described in their papers.

Here, we only briefly introduce the method. Basically, the inverse method introduces a stream function to reconstruct the 2D depth-averaged current field within the tomography area. Consequently, the inverse issue resolves the unknown stream function based on the observation data recorded by FAT, and random errors are included in it. Thus, the inverse problem can be expressed in matrix notation as

$$y = Ex + e \tag{1}$$

Here, matrix y indicates the travel time difference for the actual station pairs, matrix E is the transform matrix that mainly rest with the FAT positions in the tomography area, x represents the unknown solution vectors for the Fourier expansion of the stream function, and e is the random error vector, corresponding to the observation and inverse method errors.

In order to decrease the periodicity effect in the solution, the inversion area should be adopted larger than the tomography area (Park & Kaneko, 2001). In this study, the inversion domain was set to 620 m length by 340 m width (Figure 1c). The number of truncated Fourier series coefficients was set to 3 in this study.

To consider the riverbank condition in the inverse problem, a set of linear equations $0 = \mathbf{u}(x_b, y_b)\cdot\mathbf{m}(x_b, y_b)$ were established, where **m** represents the unit vector perpendicular to the riverbank at each given position (x_b, y_b). Then, the linear equations were rewritten by the stream function, and these equations were added to the rows of Equation 1. Here, the riverbank condition was given at 22 points distributed over each riverbank, as seen in Figure 1c. Equation 1 is solved by the damped least-squares method clarified by Yamoaka et al. (2002) and Yamaguchi et al. (2005).

3. Results

3.1 Typical ray simulation results

Figure 3 demonstrates the ray patterns attained between the shortest station pairs (S1-S2, ~ 85 m) and the longest station pairs (S3-S6, ~ 322 m) by the ray-tracing method. Figure 3a demonstrates the typical vertical profiles of salinity, temperature, and sound speed documented by CTD at the upstream Misasa Bridge at high water. Owing to saltwater intrusion, deeper water had a higher salinity and temperature. The sound speed remained fairly constant at the upper levels, while at deeper levels, the sound speed showed a greater range, varying from 1450 to 1475 m/s.

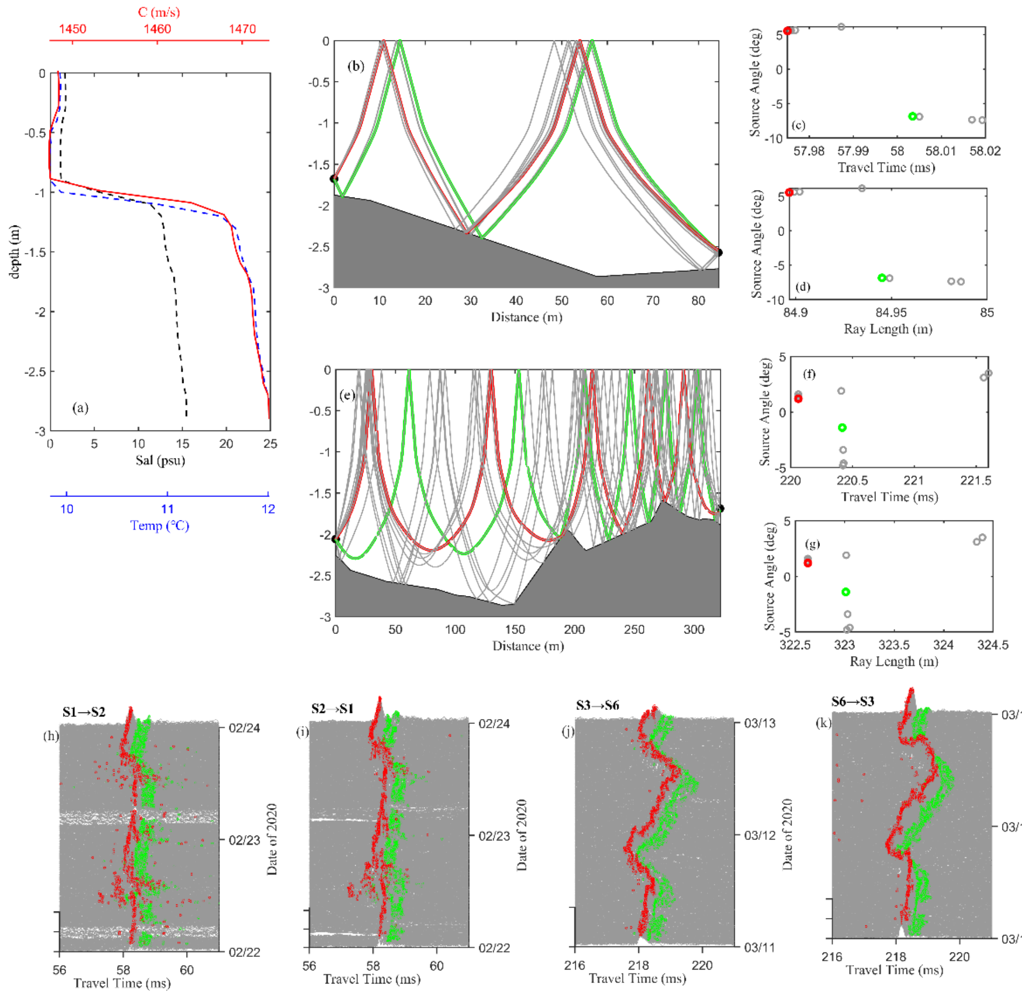

Figure 3. (a) Typical water temperature vertical profile, salinity vertical profile, and calculated sound speed vertical profile. (b)–(d) and (e)–(g) display the results of ray tracing along the shortest and longest transmission lines S1-S2 and S3-S6. (h), (i), (j), and (k) are elected stack graphs of the received correlation shapes drawn with the time axis (ms) along the shortest and longest transmission lines S1-S2 and S3-S6.

Rays with large launch angles make multiple bottom and surface reflections; for example, surface-bottom reflected rays with large angles caused the number of reflections to be more than 7 for the longest line S3-S6, and did often not arrive at the receiver because of the large transmission losses. Only the rays launched with small angles were successfully traced to simulate the sound traveling processes. The simulated values were roughly similar to the observed results. The rays launched with a positive angle that were linked to the first/largest arrival peak with a few surface-bottom reflections are marked with red lines (Figures 3b and 3e). Thus, the first peak points were selected as input data in the inverse analysis in this study (Figure 3).

3.2 Inverse results

3.2.1 Depth-averaged tidal current distributions

The behaviors of the 2-hour interval 2D depth-averaged tidal currents (Figure 4) were reconstructed applying the inverse approach from 22 February to 24 February. The flow distribution pattern varied well with the tide, and the inversed velocity directions and magnitudes exhibited well agreement with those measured by the fixed ADCP near stations S1, S3, and S5. The temporal-spatial distributions of the tidal currents appeared realistic, considering the bathymetry and shape of the surveyed area (Figure 1). The currents tended to be slow and divided into two parts in the area around the confluence location (S5). During flood tide, significant landward currents flowed with a maximum speed value of 0.35 m/s; and during ebb tide, significant seaward currents were observed, with a maximum speed of 0.45 m/s. Temporally, the current distribution at the tidal junction showed that tidal currents during ebb tide were higher than during flood tide. Spatially, the behaviors of velocity distribution at the tidal junction indicated that tidal currents in the Kyu Ota River (eastern) region are stronger than those in the Tenma River (western) region. The flow directions in the study area can be explicated by the geometry of the junction, which leads to a large curvature in the current directions when flowing into the physical domain. Generally, as shown in Figure 4, streamlines within the tomography area tended to obey the curvature of the riverbanks.

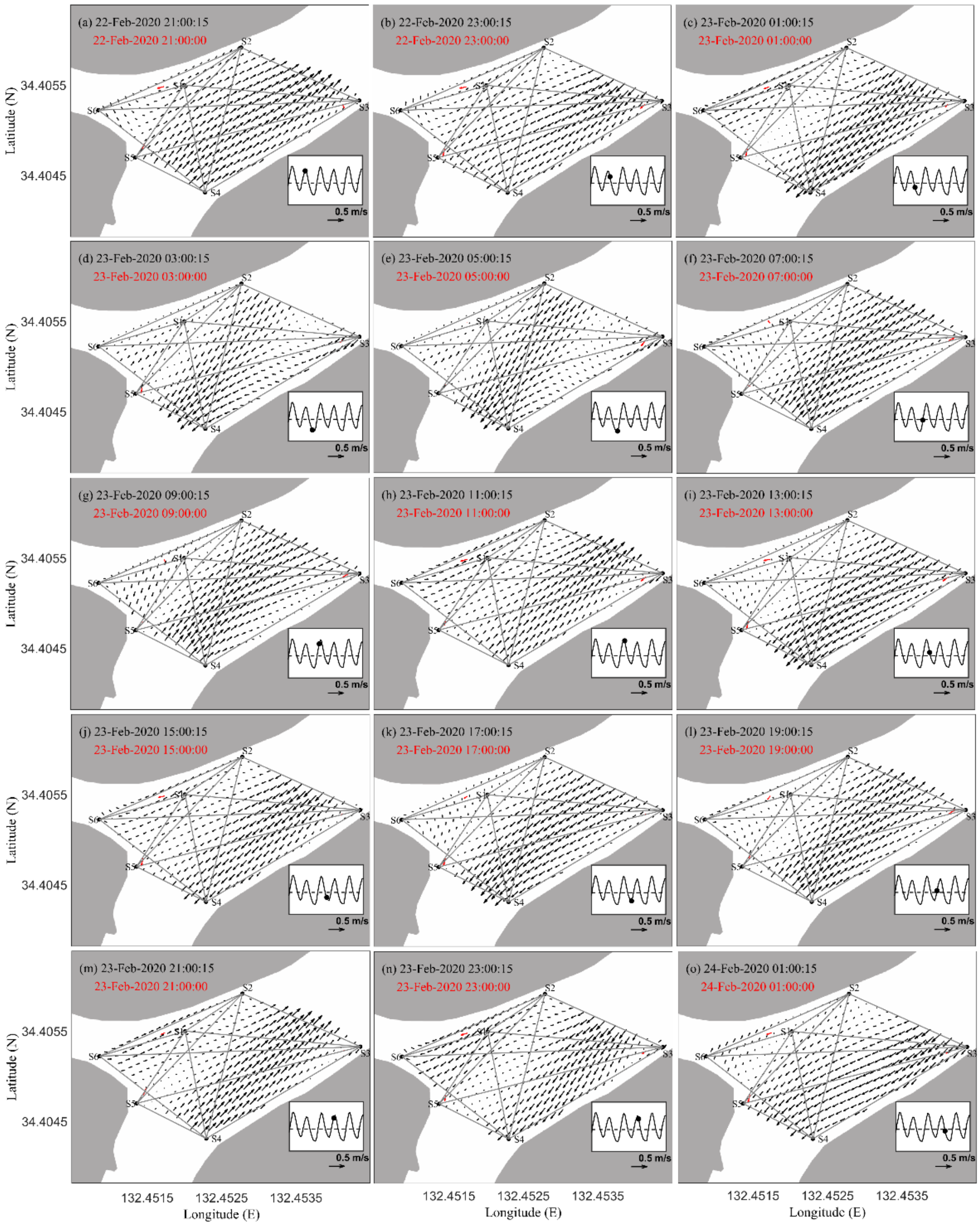

Figure 4. Depth-averaged current distributions from 22 February to 24 February, 2020, at a 2-hour interval. The black and red arrows represent the velocities acquired by FAT and ADCP, respectively. The FAT stations are marked by black dots, and the actual acoustic transmission rays among the FAT stations are connected by the solid lines. The tidal phase of each sub-figure is signaled by a black dot on the water level at the lower right corner.

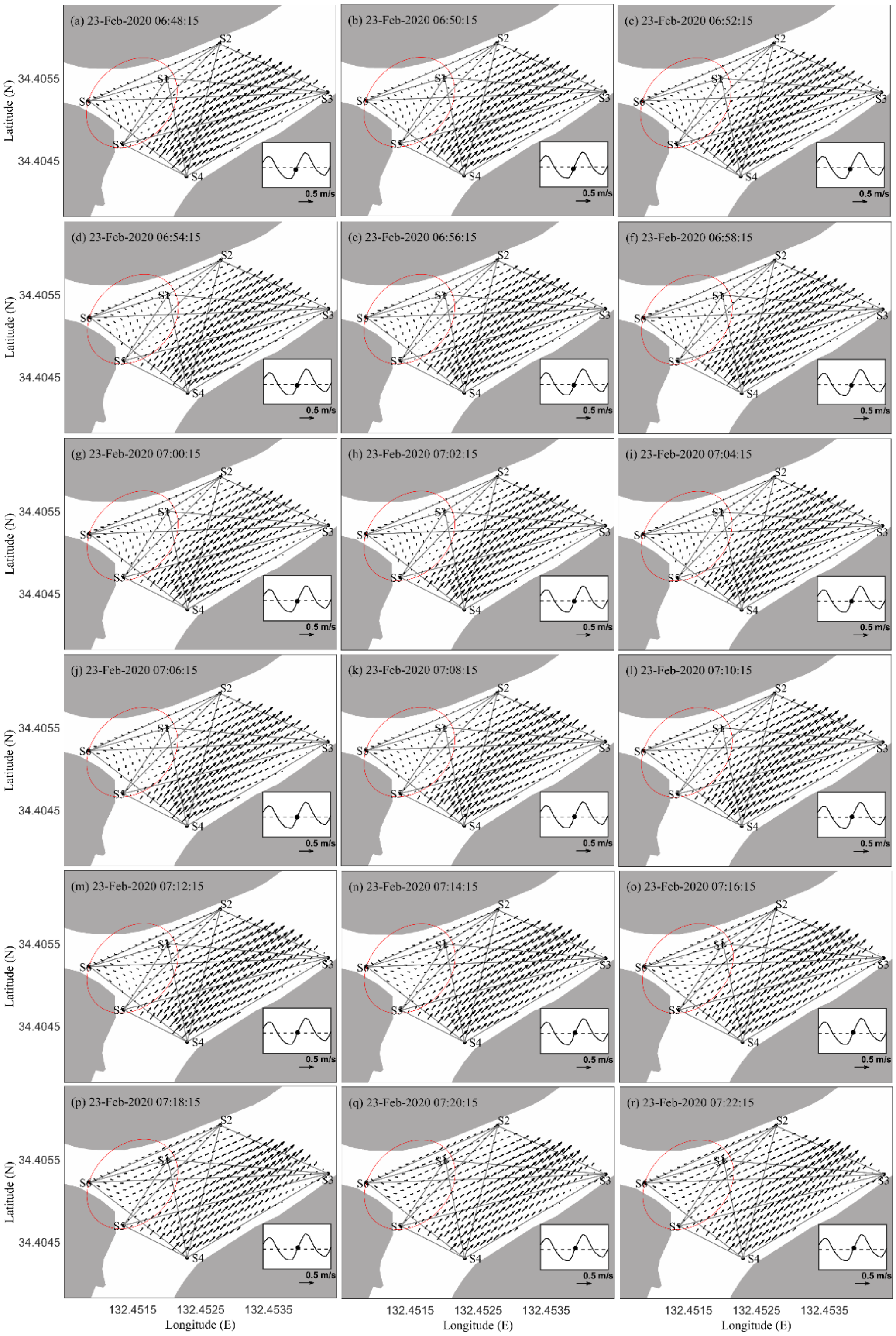

Figure 5. Depth-averaged current distributions at 2-min intervals during flood tide. The FAT stations are marked by black dots, and the actual acoustic transmission rays among the FAT stations are connected by the solid lines. The tidal phase of each sub-figure is signaled by a black dot on the water level at the lower right corner.

In this study, the high frequency observation interval (1-min) provided the opportunity to explore the detailed processes of the formation of tidal current structures at the junction. In Figure 5, 2-min interval snapshots are presented during the flood tide around the higher tidal velocity. During the early flood tide period, significant landward currents flowed into the Kyu Ota River region. Meanwhile, the flow patterns marked within the red ellipse were weak compared with those in the Kyu Ota River region and flowed seaward (Figure 5a-5k). During the later flood tide period, the current patterns marked within the red ellipse were close to the velocities in the Kyu Ota River region and flowed landward (Figure 5l-5r). As shown in Figure 5, from Figure 5k to Figure 5p within the red ellipse, it took almost 12 min to complete the transformation of flow patterns. The dynamics of the flow patterns will be discussed later in this paper.

3.2.2 Comparison of FAT and ADCP results

Further, to verify the performance of the tomographic results, we compared the inverse estimates with the fixed ADCP data. As shown in Figure 6, the magnitudes and directions of the velocities reconstructed by FAT were agreement with to the fixed ADCP velocities (Figure 6). The RMSE values at S1, S3, and S5-ADCP were from 0.08 to 0.17 m/s and 0.05 to 0.17 m/s for the eastward and northward components, respectively. The coefficients of determination (R^2) of both components at S1, S3, and S5-ADCP were from 0.61 to 0.67 and 0.55 to 0.67, respectively. The large RMSE values related to S3-ADCP show an underestimation of the eastward components, which may result from the reason that the fixed ADCP monitors much smaller spatial scales of velocities. The ADCP sites did not overlap with any of the computational grid nodes, the generated velocities are the averaged values from the nearby points within the computational area that surrounded each fixed ADCP.

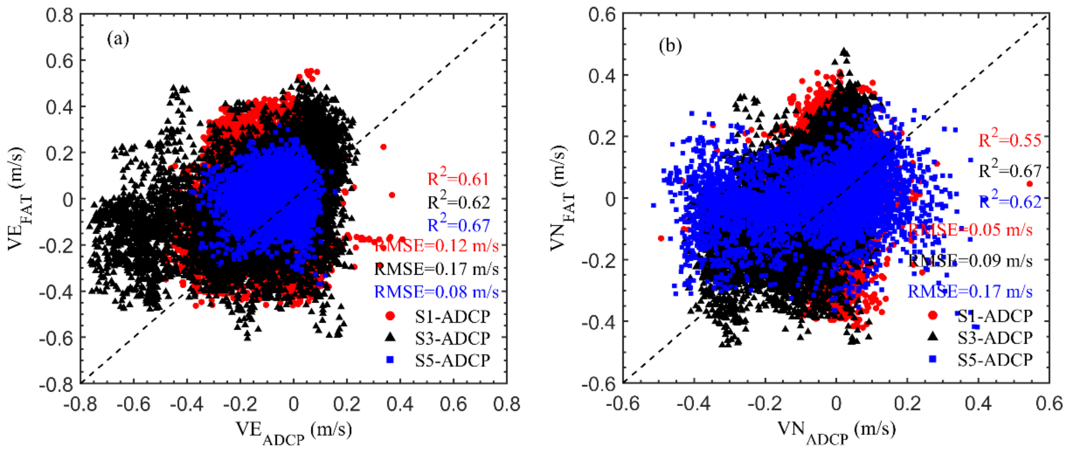

Figure 6. Relationships between FAT and ADCP are shown (a) eastward and (b) northward velocity components. The coefficient of determination (R^2) and the root mean square error (RMSE) are given at the right side of each panel.

Moreover, Figure 7 compares the depth-averaged velocity directions obtained from moving-boat ADCP measurements against those derived from FAT. Despite the fundamental and essential differences between these two techniques, the behaviors of tidal velocity shown in Figure 7 indicate that there is a well agreement between these two different techniques at the tidal junction.

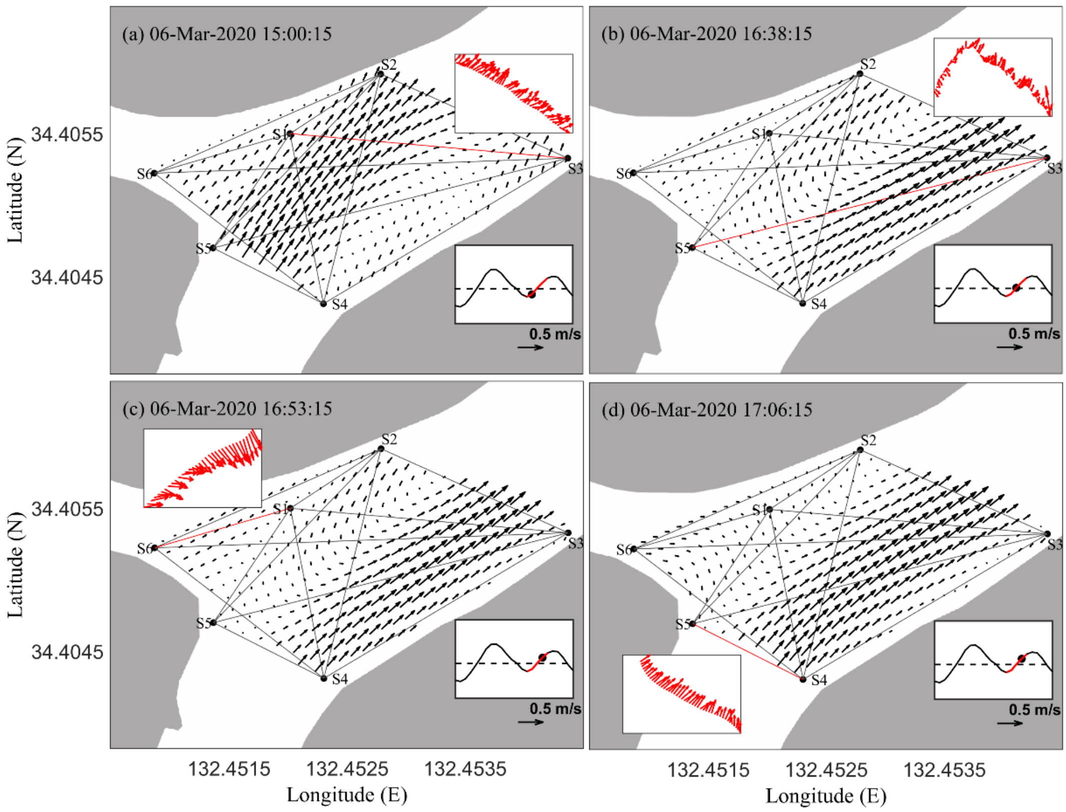

Figure 7. Typical Depth-averaged current structures from FAT during the StreamPro ADCP observation period. The red solid lines connecting the acoustic stations represent the StreamPro ADCP observation routes. The velocity directions along the ADCP routes are shown in the sub-figure of each panel. The tidal phase of each sub-figure is signaled by a black dot on the water level at the lower right corner.

3.3 Tidal distortion and asymmetry at the junction

In estuarine systems, due to the interactions of tidal harmonics, the tidal response is generally described by the progress of tidal distortion and asymmetry. The M_2 and M_4 tides are the most crucial astronomical and shallow-water components, respectively. Hence, Friedrichs and Aubrey (1988) proposed a mathematical relationship between M_2 and M_4, which is utilized as the indicators of tidal distortion and asymmetry. The inverse method calculates the depth-averaged velocity at each computational grid point. Thus, the inversed velocity results with 1-min intervals were directly applied to a point-by-point classical tidal harmonic analysis to acquire the M_2 and M_4 tidal constituents (Pawlowicz et al., 2002).

Figure 8 shows the spatial distributions of these two indicators at the junction. The distorted tide had an M_4/M_2 amplitude ratio greater than zero (Figure 8a); the larger the values of the M_4/M_2 amplitude ratio, the more significant the tidal distortion. The mean flood and ebb durations at Misasa gauging station were around 5.5 h and 6.9 h, respectively, with a 1.4 h difference in tidal durations. The velocity phase of $2M_2$-M_4 showed both types of asymmetric distortion at the junction (Figure 8b). From the Tenma River region to line S1-S5, the velocity phase indicator indicated an ebb-dominant asymmetric distortion. The type becomes a flood asymmetry in the Kyu Ota River region. As presented in Table 1, the results of the velocity data of three fixed ADCP stations confirmed the same type of asymmetric distortion at the three positions. Flood-dominated systems usually refer to the asymmetry characteristics of the flood duration is shorter than the ebb duration in tidal water levels and the higher flood velocity during flood tide larger than that during the ebb tide (Friedrichs & Aubrey, 1988). In ebb-dominated systems, the relationship is reversed.

The two indicators reflect the combined effects of tidal energy transfer and frictional dissipation at the junction. The ebb dominance type in the Tenma River region is mainly a result of extensive tidal flats. The tidal flats cause higher bed levels in the Tenma River region than in the Kyu Ota River region and lead a slower rate of non-linear growth of M_2 (Friedrichs & Aubrey, 1988).

Table 1. Amplitude and phase of M_2 and M_4 of the velocity data of the three fixed ADCP stations obtained by harmonic analysis.

	M_2		M_4			
	Amplitude (m/s)	Phase (°)	Amplitude (m/s)	Phase (°)	M_4/M_2	$2M_2$-M_4 (°)
S1-ADCP	0.0795	35.63	0.0162	284.93	0.21	-213.67
S3-ADCP	0.1003	33.53	0.0318	281.66	0.32	-214.60
S5-ADCP	0.1135	60.57	0.0115	85.28	0.11	35.86

The tidal harmonic length analyses at S1-ADCP, S3-ADCP, and S5-ADCP were performed from February 21 to March 9, February 21 to March 13, and February 21 to March 7, respectively.

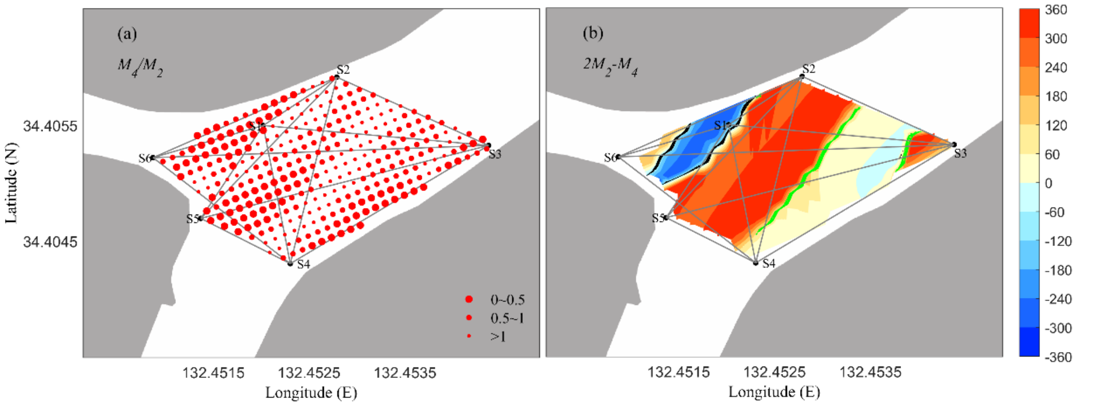

Figure 8. Distributions of (a) the M_4/M_2 ratio of the velocity amplitudes, and (b) the $2M_2$-M_4 of velocity phase in degrees. The green (black) lines in (b) represent the 90°

(-90°) contour lines.

4. Discussion

4.1 Evaluation of the inversion results

The spatial resolution ΔR (ΔR=$\sqrt{\frac{A}{N}}$) is decided by the number of acoustic transmission rays within the tomography area (Park & Kaneko, 2001). A represents the tomography area (~52700 m^2), and N is the amount of successfully transmitted rays (N <= 14). The highest spatial resolution of the acoustic array was around 7.8 m in this work.

During the damped least-squares method, the damping factor α was used to stabilize the inverse analysis solutions (Yamaguchi et al., 2005; Yamoaka et al., 2002). For the damped least-squares method, the expected error covariance matrix U (uncertainty) of the solutions can be written as

$$U = I - E^T(EE^T + \alpha^2 I)^{-1}E \quad (2)$$

By multiplying the vector P comprised the harmonic functions emerging in the Fourier series, matrix U is converted into S in a physical area:

$$S = P^T UP \quad (3)$$

The diagonal elements of S represent the uncertainties of the inverse analysis solutions in the tomography domain. The amount and layout of successfully transmitted rays and the values of the damping factor α calculated by the L curve method mainly regulate the uncertainties.

Regarding the specificity of the study area, the reciprocal sound transmissions related to S5 and S6 are important to obtain the inverse results. Here, we conducted several cases to discuss the uncertainties of the inverse results.

Case I (N=14): In most of the inverse area, the uncertainties were less than 0.1 m/s in the tomography domain (Figure 9a, 9b). Higher uncertainties were always exhibited around S4 and at the center of the tomography domain (Figure 9a, 9b). Case II (lack of S4-S6): similar to Case I, most of the values were less than 0.1 m/s (Figure 9c, 9d). Case III (lack of S4-S6, S1-S5, S2-S5, and S3-S5) and Case IV (lack of S4-S6, S1-S5, S2-S5, S3-S5, S1-S6, S2-S6, and S3-S6) showed a significant increase in uncertainties. Specifically, the uncertainties showed a dramatic increase when the case changed from Case III to Case IV. The spatially averaged uncertainties of a (Case I, high water), b (Case I, low water), c (Case II, low water), d (Case II, high water), e (Case III, low water), f (Case III, high water), g (Case IV, low water), and h (Case IV, high water), followed the proportions of 1.0: 1.1: 1.29: 1.22: 2.23: 1.91: 3.23: 3.98.

Under ideal conditions, observations with more FAT stations and higher frequencies will acquire more precise results at the shallow tidal junction. Zhang et al. (2017) conducted an experiment with 11 coastal acoustic tomography (CAT) systems in Dalian Bay to discuss the tidal current structures. The precision of their observations was the highest thus far because of the largest number of transmission rays (51) that ever recorded in the previous studies, but the observation period was limited to one day. The related data in Section 3.2 show satisfactory results for the current distribution. However, the successful acquisition rates of the 14 sound transmission rays had a wide variation (19%–92%, Figure 2b). Overall, this study scheme performed well (considering observation period and precision) adjacent to the tidal junction.

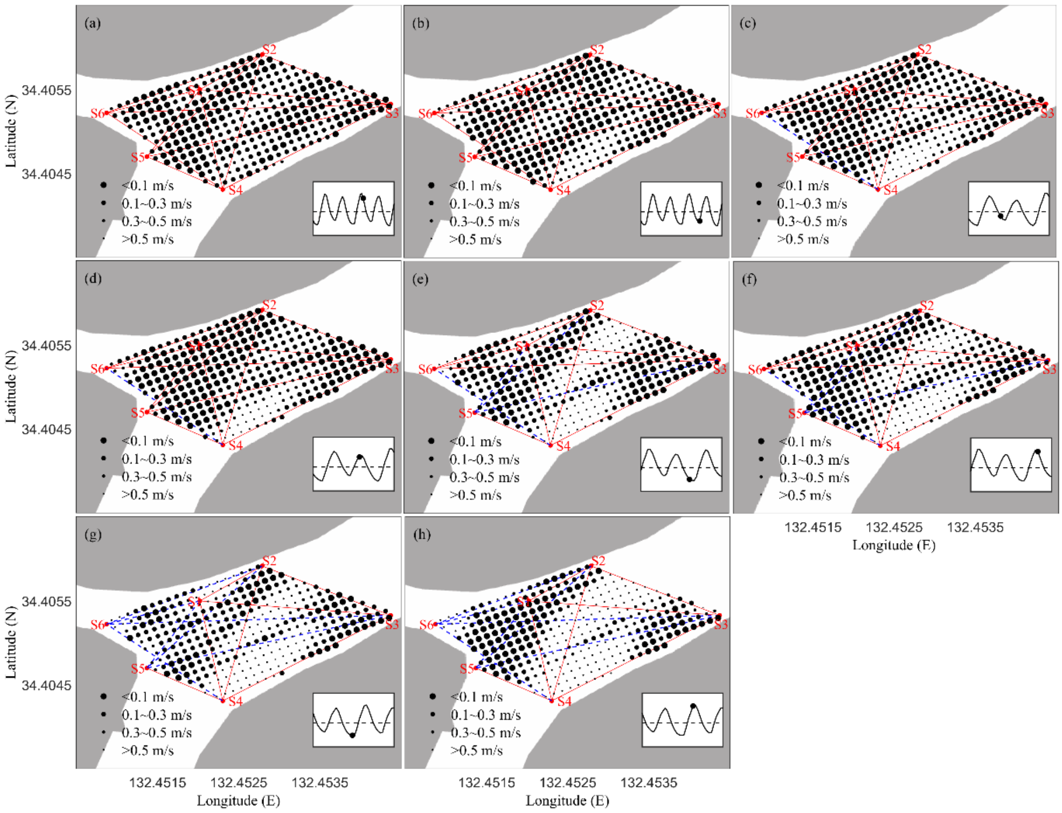

Figure 9. Uncertainty maps for inverse solutions of some typical cases.

4.2 Dynamic mechanisms of tidal currents at the junction

As shown in Section 3.2.1 (Figure 5), the transformation of flow patterns took place during the flood tide in the area around the confluence location (S5). To understand the processes of flow pattern formation, we calculated the relative vorticity ($\zeta = \frac{\partial v}{\partial x} - \frac{\partial u}{\partial y}$, u and v represent the eastward and northward velocity components inversed by FAT, respectively) during the flood tide at the junction.

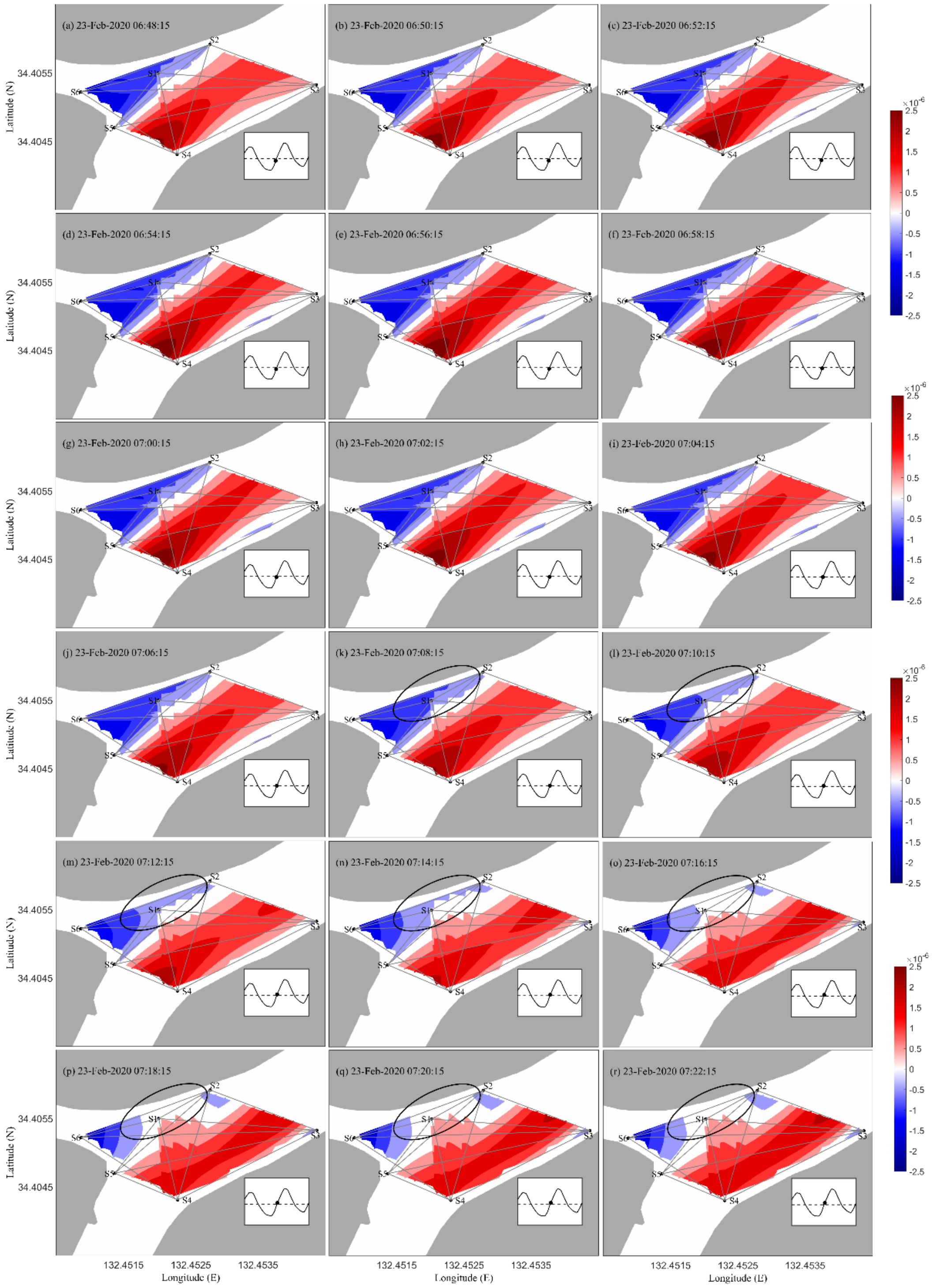

Figure 10. Maps of the relative vorticity during the flood tide corresponding to the horizontal current distributions in Figure 5.

As shown in Figure 10, positive and negative ζ appeared in the Kyu Ota River and Tenma River regions, respectively. This results from the geometry of the junction. The tide in the Tenma River region is dominated by a west-eastward direction, while it is dominated by a northeast-southwestward direction in the Kyu Ota River region. The flow patterns exhibited transformations of the current (Figure 5k to Figure 5p) and vorticity patterns (Figure 10k to Figure 10p). The area with negative ζ values (blue) gradually decreased, while the area with positive ζ values (red) gradually extended to lines S1-S2 (Figure 10k-10p). Danial et al. (2019) indicated that the Tenma River is more convergent than the Kyu Ota River, resulting in a larger phase difference in the tidal discharge/tidal velocity at the Tenma River. Additionally, Danial et al. (2019) revealed that the tidal discharge phase at the Tenma River was ahead by ~15-min as compared with that at the Kyu Ota River. The tidal discharges were well related to the tidal velocities. The nonlinear effect leads to some differences when the tidal wave propagates from the river mouth to the junction through these two different branches during the flood tide. The phase difference (φ) and phase lag (ε) have a relationship with $\varepsilon + \varphi = \frac{\pi}{2}$. Thus, it can be inferred that the transformation of the tidal current patterns during flood tide results from the phase difference/phase lag. The quick processes of decay and transformation of tidal current patterns are a difficult target for the fixed ADCP or moving-boat ADCP; however, the FAT observations allow us to investigate such patterns. This study further demonstrates the fascinating application (continuous measurement of 2D flow pattern) of FAT in shallow water environments.

The flow directions in the survey area can be explained by the geometry of the junction. The geometry of the junction results in a large curvature in the flow directions when the flow enters the tomography domain. Overall, as shown in section 3.2, streamlines tend to follow the shape of the riverbanks.

4.3 Tidal propagation and damping at the junction

Based on the harmonic analysis of the water level (Table 2), we selected 13 significant tidal constituents to discuss the propagation and dampening process of the tide at the junction. The inversed velocity data with 1-min intervals were applied to a point-by-point classical tidal harmonic analysis to acquire the 13 tidal constituents. The spatial variabilities of the 13 tides are presented in Figure 11. The spatially averaged tidal current amplitudes of *Mm*, *MSf*, K_1, O_1, Q_1, M_2, S_2, N_2, L_2, M_4, MS_4, M_6, and M_8, followed the proportions of 1.00: 0.72: 0.62: 0.48: 0.33: 2.78: 1.42: 0.66: 0.84: 0.25: 0.60: 0.25: 0.20.

Table 2. Amplitude and phase of 13 significant tidal components at Eba and Misasa gauging stations obtained by tidal harmonic analysis of 35 days of water level data.

	Eba		Misasa	
Tidal Constituent	Amplitude (m)	Phase (°)	Amplitude (m)	Phase (°)
Mm	0.0569	12.77	0.1417	22.29
MSf	0.0180	308.71	0.0932	0.0932
K_1	0.2269	233.53	0.1855	231.69
O_1	0.2225	186.33	0.1770	183.72

Q_1	0.0532	166.03	0.0336	173.36
M_2	0.9867	274.33	0.8560	279.10
S_2	0.5274	324.92	0.4275	326.98
N_2	0.2077	265.39	0.1529	274.26
L_2	0.0833	294.64	0.1466	299.23
M_4	0.0170	43.60	0.0712	165.05
MS_4	0.0248	97.28	0.0634	213.82
M_6	0.0225	136.87	0.0149	230.16
M_8	0.0001	242.52	0.0100	92.99

As shown in Figure 11, low-frequency tides became stronger at the tidal junction. The monthly tide (*Mm*, T≈27.6 d) and the fortnightly tide (*MSf*, T≈14.8 d) were more significant than diurnal tides. Godin (1999) showed that in a tidal river, most linear tidal components will be damped more quickly than M_2, while some tidal constituents might be enhanced by nonlinear energy transfer or resonance. The M_6 and M_8 tide constituents were insignificant compared to other shallow-water constituents and remained constant at the junction (Figures 11l and 11m). The variations in the tidal currents at the junction were dominated by semidiurnal species (D2: M_2, S_2, N_2, L_2), followed by diurnal species (D1: K_1, O_1, Q_1) and quarter-diurnal species (D4: M_4, MS_4). This indicates that at the junction, the shallow water effect does not trigger the tidal distortion of D2 well; thus, it cannot generate sufficient energy to convert D2 to D4. Here, the surveyed tidal channel junction is situated only 5.8 km upstream from the estuary, implying that the tide should propagate more to upriver areas to generate D4.

Tidal characteristics can be recognized using the form number (Pugh, 1987), and it is determined by the amplitude ratio between the main diurnal and semidiurnal tidal constituents ($F=(a_{K1}+a_{O1})/(a_{M2}+a_{S2})$). The form number of the water level at the Eba and Misasa gauging station was 0.29 and 0.28, indicating that the tide is of a mixed type. The form numbers of tidal velocity varied at the junction (Figure 11n), mostly between 0.25 and 1, with higher values in the Kyu Ota River. The form number indicated that the tidal regime at the junction can be deemed to be of a mixed type.

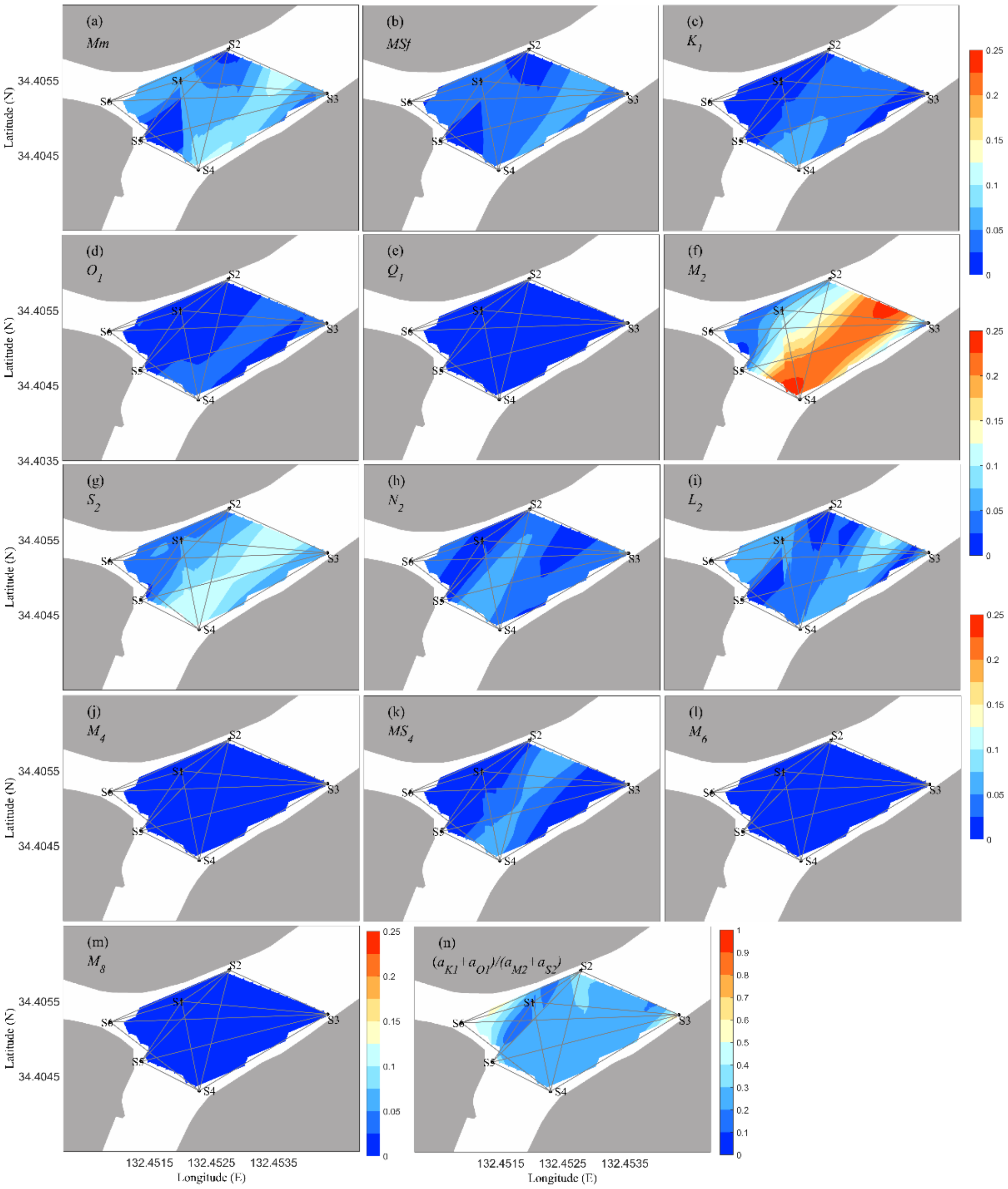

Figure 11. (a)–(m) distributions of the amplitude of the 13 tidal components (*Mm*, *MSf*, K_1, O_1, Q_1, M_2, S_2, N_2, L_2, M_4, MS_4, M_6, and M_8) at the junction; (n) amplitude ratio $((a_{K1}+a_{O1})/(a_{M2}+a_{S2}))$ between the main diurnal and semidiurnal tidal constituents.

Nontidal forcing (e.g., river discharge) contributes to sub-tide species, affecting tidal lists to remove these tide constituents as contaminated by noise (Ray & Erofeeva, 2014). For example, In the Yangtze River Estuary, Guo et al. (2015) reported that river discharge can strongly induce substantial annual mean water level differences and related differences in tidal amplitudes; however, river discharge restricted variations in the monthly and fortnightly tidal frequencies. In other words, interactions between tidal components are an important reason for tidal low-frequency variations in tide propagating processes and generated low-frequency tides. The interaction of M_2 and S_2

caused fortnightly (*MSf*) variations in tidal properties (ω_{M2}-$\omega_{S2=}\omega_{MSf,}$ ω is tidal frequency); the interaction of M_2 and N_2 caused monthly (*Mm*) tidal variations (ω_{M2}-$\omega_{N2=}\omega_{Mm}$). The production of such compound tides suggests a tidal energy transfer from semidiurnal frequencies to sub-tide frequencies (Gallo & Vinzon, 2005). Similar interactions also exist between other semidiurnal and diurnal tides. Usually, the tidal potential includes limited energy at the *MSf* and *Mm* tidal frequencies, and becomes negligible in the upstream areas of a river (Zhang et al., 2012). But, as shown in Figures 11a and 11b, the *MSf* and *Mm* tides grew strongly. During low-flow days, the freshwater discharge in the upriver only varies between 20 and 50 m^3/s (Danial et al., 2019). The role of freshwater discharge at the junction is negligible during low-flow periods. Thus, fortnightly and monthly subtidal variations at the junction are mainly controlled by the tidal interactions; they are also mediated by river flow but not directly at the junction.

While the tides propagate along the channel, the tidal dampening process is dramatically affected by the friction effect, followed a decreased tidal range in space. In this study, owing to the lack of temporal-spatial distributions of tidal ranges along the channel, we only compared the tidal range between two gauging stations (Eba, Misasa). As shown in Figure 12b, fortnightly variations in tidal ranges were evident at both the Eba and Misasa stations, and a decreasing trend of the tidal ranges was manifested along the channel. In convergent estuaries, the enhancement and attenuation of tidal energy are considerably governed by the relative intensity of dissipation versus local inertia in the momentum equation, also the function of channel convergence in the mass balance (van Rijn, 2011). On the other hand, strongly convergent shallow estuaries was investigated by Friedrichs and Aubrey (1994), the findings indicated that they are dynamically controlled by friction and kinematically influenced by convergence. As the channel convergence increases, the characteristics of tidal distortion are increased, alternatively speed and wavelength of tidal wave significantly decrease (Lu et al., 2015). In the case of weakly dissipative estuaries, tide propagation feature can be described by a feebly nonlinear behavior, and over-tides are produced in a cascade process, so that the higher harmonics have progressively reduced amplitudes (Lanzoni & Seminara, 1998). For this study, although the shallow water depth and convergent width might increase the tides to some degree, the declining trend during the spring tide suggests that the tidal channel is a strongly dissipative channel accompanied by strong nonlinear effects.

4.4 River-Tide interactions at the junction

River flow significantly influences tidal dynamics by decreasing the tidal amplitudes, obstructing wave propagation, and modifying the tidal energy distribution between tidal frequencies (Sassi & Hoitink, 2013). Theoretical analysis suggests that a tidal channel with constant depth and width causes a roughly linear relationship between tidal damping coefficients and streamflow, and the amplitude of the incident wave from the estuary to the upstream areas varies with the square root of river flow

(Jay & Flinchem, 1997). However, the tidal damping process is nonlocal. Therefore, the independent impacts on tidal damping induced by a varying river flow are not easy to quantify (Kukulka & Jay, 2003).

River flow also modifies the interactions between tidal constituents and the subsequent generation of over-tides and compound tides. This process is clearly revealed by the reduced M_4 amplitude during high flow periods, whereas the amplitude ratio of the M_4/M_2 was larger during low flow periods (Figure 12d). This reflects the more significant tidal wave deformation that occurred during the high flow periods. River flow plays a crucial role in river flow enhanced subtidal friction, which significantly diminishes the tidal energy at the upstream whilst triggering tidal energy transfer from the primary tides to over-tides at the downstream (Cai et al., 2014).

Additionally, river-tidal interactions significantly disturb the characteristic of tidal asymmetry. Some studies observed a landward increase in the amplitude of the M_4/M_2 ratio with a damping of the M_2 tide and noted a significant decline in the amplitude of the M_4/M_2 ratio from spring to neap tide (Guo et al., 2015; Lu et al., 2015). In this work, we also found larger M_4/M_2 amplitude ratios during spring than that during neap tide (Figure 12c), indicating that the M_2 tide progressively transformed to the M_4 tide from neap tide to spring tide.

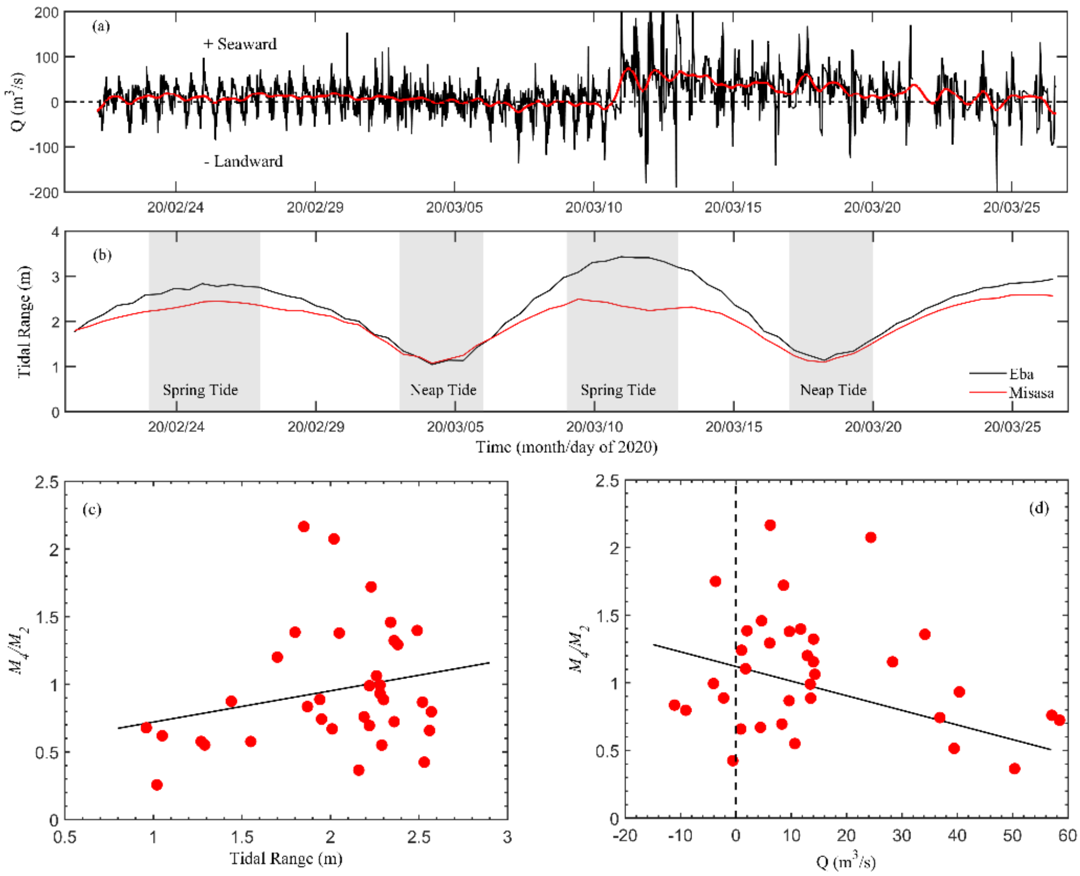

Figure 12. (a) tidal discharge in the Kyu Ota River; the tidal discharge was calculated from the transmission line S2-S3 (Figure 1b); (b) tidal ranges at two water level gauging stations (Eba and Misasa); (c) relationship between the daily spatially

averaged amplitude of the M_4/M_2 ratio and daily tidal range; and (d) relationship between the daily spatially averaged amplitude of the M_4/M_2 ratio and daily river discharge.

The nonlinear tide M_4 and its related tidal asymmetry are one of the most important mechanisms causing residual suspended sediment transport in estuarine environments (Hoitink & Jay, 2016). For this study, at the tidal junction of the Ota River estuarine system, river flow is limited during the normal situation, so that the influences resulting from tide-induced asymmetric currents are noteworthy for suspended sediment transport (Xiao et al., 2020). This is different from the situation in the Yangtze River estuary because of river discharge is so strong (6000–92000 m^3/s) that the enhanced ebb-directed sediment transport by the river flow is significant, while the roles of tide-induced asymmetric currents are negligible in suspended sediment transport mechanisms (Guo et al., 2014). The interactions between river and tide and the resultant tidal asymmetry are crucial at the junction or at the Ota River estuary. They may cause significant variations in water levels and bed frictions, which have continuous effects on the process of erosion, deposition, and transport of sediment. Here, we estimated the bed friction from tidal currents, following the basic equations shown in Cea and Vázquez-Cendón (2012). Temporally, a higher bed friction occurred during the spring periods than during the neap periods. Spatially, bed friction at the junction showed that values in the Kyu Ota River were higher than those in the Tenma River (Figure 13). The bathymetry distribution revealed that the eastern channel region is deeper than the western channel region at the junction, which demonstrates the role of bed friction. Bed friction plays a fundamental role in sediment motion and moderately modifies the basin geometry and bathymetry.

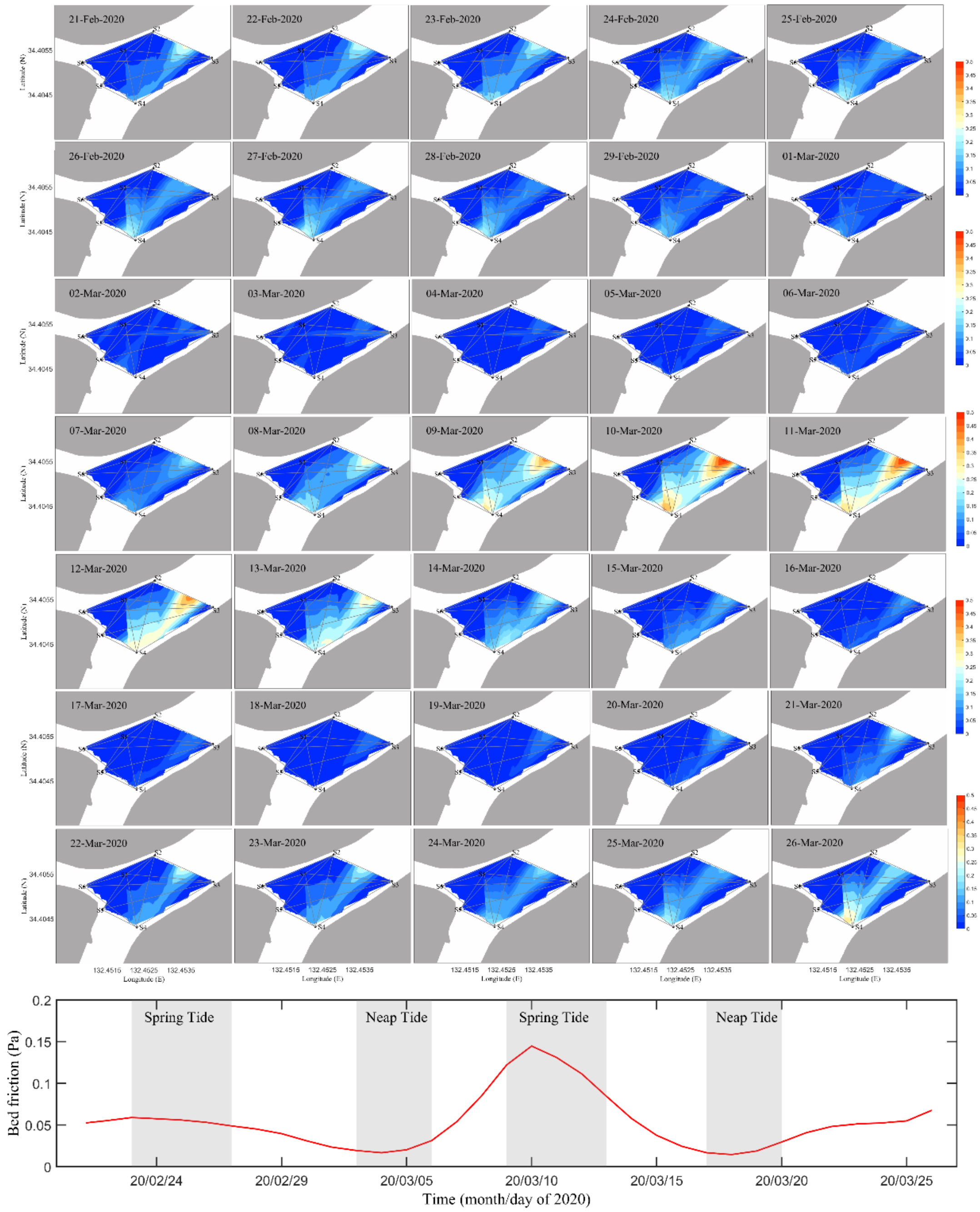

Figure 13. Daily bed friction (Pa) distribution estimated from tidal currents and variations in the daily spatially averaged bed friction from 21 February to 26 March, 2020.

5. Conclusions

For the first time, continuous 2D tidal current fields were measured at a shallow junction using fluvial acoustic tomography (FAT) systems composed of six fixed acoustic stations from February 21 to March 26, 2020. The horizontal structure and the spatiotemporal variation of the tidal velocities were well revealed by FAT. In total, actual reciprocal sound transmissions were performed during ~ 34.4 days along 14 transmission lines. The horizontal tidal velocities estimated by inverse analysis agreed well with the fixed ADCP and the moving-boat ADCP velocities.

Temporally, tidal currents during ebb tide were higher than during flood tide. Spatially, tidal currents in the Kyu Ota River region were stronger than those in the Tenma River region. Tidal currents tended to be slow and separated into two parts in the area around the confluence location. The high frequency observation interval (1-min) used in this study provided an effective way to detect the rapid processes of the transformation of tidal current patterns during flood tide at the junction. These results demonstrate that FAT is a fascinating tool for continuously mapping variable 2D tidal current structures at shallow tidal junctions. Furthermore, several case studies were performed to appraise the influence of the acoustical ray number and bathymetry on the inverse results. Overall, this work showed a good performance of the employed methods (observation period and precision) at the tidal junction. The velocity amplitude ratio of M_4/M_2 showed that the tidal distortion was significant at the junction, and the velocity phase of $2M_2$-M_4 indicated both two types of asymmetric distortions at the junction.

The tidal harmonic analysis method was adopted for the tidal currents reconstructed by the inversion of the FAT data. Further, the comprehensive evolution processes of tidal asymmetry, tidal distortion, tidal dampening, and tidal propagation at the junction were studied and discussed. The spatial distributions of 13 tidal constituents allowed to clearly disentangle the evolution process of sub-tide species (*Mm*, *MSf*), semidiurnal species (D2: M_2, S_2, N_2, L_2), diurnal species (D1: K_1, O_1, Q_1), and quarter-diurnal species (D4: M_4, MS_4). The ratios of the tidal current amplitudes of *Mm*, *MSf*, K_1, O_1, Q_1, M_2, S_2, N_2, L_2, M_4, MS_4, M_6, and M_8 were 1.00: 0.72: 0.62: 0.48: 0.33: 2.78: 1.42: 0.66: 0.84: 0.25: 0.60: 0.25: 0.20, respectively.

This study demonstrated that the application of FAT in conjunction with the inverse method presents an effective tool to map 2D tidal currents and to investigate the propagation and damping of tidal currents in a shallow tidal junction in detail.

Acknowledgments

Cong Xiao is very thankful for the China Scholarship Council (CSC) in supporting his doctoral course at Hiroshima University. This work was financed by the Japan Society for the Promotion of Science (JSPS) KAKENHI grant number JP17H03313. We acknowledge the students who joined us during the field work for their assistance with data collection. We would like to thank Dr. Chuanzheng Zhang (State Key Laboratory of Satellite Ocean Environment Dynamics, Second Institute of Oceanography, State Oceanic Administration, China), and Dr. Minmo Chen and Professor Arata Kaneko of Hiroshima University for their valuable suggestions for analyzing the data. Also, we are thankful for Editage (www.editage.com) for its assistant given for the English language.

The water level data at Misasa and Eba gauging stations were download from the Ministry of Land, Infrastructure, Transport and Tourism (http://www1.river.go.jp), and precipitation data were downloaded from the Japan Meteorological Agency (http://www.jma.go.jp). The data used in this study for reproducing the figures are available by contacting Kiyosi Kawanisi, Hiroshima University (kiyosi@hiroshima-u.ac.jp).

References

Cai, H., Savenije, H., & Toffolon, M. (2014). Linking the river to the estuary: influence of river discharge on tidal damping. *Hydrology and Earth System Sciences, 18*(1), 287.

Cai, H., Yang, Q., Zhang, Z., Guo, X., Liu, F., & Ou, S. (2018). Impact of river-tide dynamics on the temporal-spatial distribution of residual water level in the Pearl River channel networks. *Estuaries and Coasts, 41*(7), 1885-1903.

Cea, L., & Vázquez-Cendón, M. E. (2012). Unstructured finite volume discretisation of bed friction and convective flux in solute transport models linked to the shallow water equations. *Journal of Computational Physics, 231*(8), 3317-3339.

Danial, M. M., Kawanisi, K., & Al Sawaf, M. B. (2019). Characteristics of tidal discharge and phase difference at a tidal channel junction investigated using the fluvial acoustic tomography system. *Water, 11*(4), 857.

Dinehart, R., & Burau, J. (2005). Repeated surveys by acoustic Doppler current profiler for flow and sediment dynamics in a tidal river. *Journal of Hydrology, 314*(1-4), 1-21.

Friedrichs, C. T., & Aubrey, D. G. (1988). Non-linear tidal distortion in shallow well-mixed estuaries: a synthesis. *Estuarine, Coastal and Shelf Science, 27*(5), 521-545.

Friedrichs, C. T., & Aubrey, D. G. (1994). Tidal propagation in strongly convergent channels. *Journal of Geophysical Research: Oceans, 99*(C2), 3321-3336.

Gallo, M. N., & Vinzon, S. B. (2005). Generation of overtides and compound tides in Amazon estuary. *Ocean Dynamics, 55*(5-6), 441-448.

Godin, G. (1999). The propagation of tides up rivers with special considerations on the upper Saint Lawrence River. *Estuarine, Coastal and Shelf Science, 48*(3), 307-324.

Guo, L., Van der Wegen, M., Roelvink, J., & He, Q. (2014). The role of river flow and tidal asymmetry on 1-D estuarine morphodynamics. *Journal of Geophysical Research: Earth Surface, 119*(11), 2315-2334.

Guo, L., van der Wegen, M., Jay, D. A., Matte, P., Wang, Z. B., Roelvink, D., et al. (2015). River-tide dynamics: Exploration of nonstationary and nonlinear tidal behavior in the Y angtze R iver estuary. *Journal of Geophysical Research: Oceans, 120*(5), 3499-3521.

Hoitink, A., & Jay, D. A. (2016). Tidal river dynamics: Implications for deltas. *Reviews of Geophysics*, *54*(1), 240-272.

Jay, D. A., & Flinchem, E. P. (1997). Interaction of fluctuating river flow with a barotropic tide: A demonstration of wavelet tidal analysis methods. *Journal of Geophysical Research: Oceans, 102*(C3), 5705-5720.

Kaneko, A., Yuan, G., Gohda, N., & Nakano, I. (1994). Optimum design of the ocean acoustic tomography system for the Sea of Japan. *Journal of Oceanography, 50*(3), 281-293.

Kawanisi, K., Razaz, M., Kaneko, A., & Watanabe, S. (2010). Long-term measurement of stream flow and salinity in a tidal river by the use of the fluvial acoustic tomography system. *Journal of Hydrology, 380*(1-2), 74-81.

Kawanisi, K., Razaz, M., Yano, J., & Ishikawa, K. (2013). Continuous monitoring of a dam flush in a shallow river using two crossing ultrasonic transmission lines. *Measurement Science and Technology, 24*(5), 055303.

Kukulka, T., & Jay, D. A. (2003). Impacts of Columbia River discharge on salmonid habitat: 1. A nonstationary fluvial tide model. *Journal of Geophysical Research: Oceans, 108*(C9).

Lanzoni, S., & Seminara, G. (1998). On tide propagation in convergent estuaries. *Journal of Geophysical Research: Oceans*, *103*(C13), 30793-30812.

Lu, S., Tong, C., Lee, D. Y., Zheng, J., Shen, J., Zhang, W., et al. (2015). Propagation of tidal waves up in Y angtze E stuary during the dry season. *Journal of Geophysical Research: Oceans, 120*(9), 6445-6473.

Munk, W., Worcester, P., & Wunsch, C. (1995). Ocean acoustic tomography, Cambridge Univ. *Pr., Cambridge UK*.

Park, J.-H., & Kaneko, A. (2001). Computer simulation of coastal acoustic tomography by a two-dimensional vortex model. *Journal of Oceanography, 57*(5), 593-602.

Pawlowicz, R., Beardsley, B., & Lentz, S. (2002). Classical tidal harmonic analysis including error estimates in MATLAB using T_TIDE. *Computers & Geosciences, 28*(8), 929-937.

Pugh, D. T. (1987). Tides, surges and mean sea level.

Ray, R. D., & Erofeeva, S. Y. (2014). Long-period tidal variations in the length of day. *Journal of Geophysical Research: Solid Earth, 119*(2), 1498-1509.

Razaz, M., Kawanisi, K., Nistor, I., & Sharifi, S. (2013). An acoustic travel time method for continuous velocity monitoring in shallow tidal streams. *Water Resources Research*, *49*(8), 4885-4899.

Razaz, M., Kawanisi, K., Kaneko, A., & Nistor, I. (2015). Application of acoustic tomography to reconstruct the horizontal flow velocity field in a shallow river. *Water Resources Research, 51*(12), 9665-9678.

Razaz, M., Kawanisi, K., Nistor, I., & Zedel, L. (2016). Depth-Averaged Flow Reconstrunction in an Extremely Shallow Estuary. *Ottawa, Canada, May 10-13, 2016*.

Sassi, M., Hoitink, A., de Brye, B., & Deleersnijder, E. (2012). Downstream hydraulic geometry of a tidally influenced river delta. *Journal of Geophysical Research: Earth Surface, 117*(F4).

Sassi, M., & Hoitink, A. (2013). River flow controls on tides and tide-mean water level profiles in a tidal freshwater river. *Journal of Geophysical Research: Oceans, 118*(9), 4139-4151.

van Rijn, L. C. (2011). Analytical and numerical analysis of tides and salinities in estuaries; part I: tidal wave propagation in convergent estuaries. *Ocean Dynamics, 61*(11), 1719-1741.

Xiao, C., Kawanisi, K., & Al Sawaf, M. B. (2020). Suspended particulate matter concentration in response to tidal hydrodynamics in a long mesotidal floodway. *Estuarine, Coastal and Shelf Science, 233*, 106525.

Yamaguchi, K., Lin, J., Kaneko, A., Yayamoto, T., Gohda, N., Nguyen, H.-Q., et al. (2005). A continuous mapping of tidal current structures in the Kanmon Strait. *Journal of Oceanography, 61*(2), 283-294.

Yamoaka, H., Kaneko, A., Park, J.-H., Zheng, H., Gohda, N., Takano, T., et al. (2002). Coastal acoustic tomography system and its field application. *IEEE Journal of Oceanic Engineering, 27*(2), 283-295.

Zhang, C., Zhu, X.-H., Zhu, Z.-N., Liu, W., Zhang, Z., Fan, X., et al. (2017). High-precision measurement of tidal current structures using coastal acoustic tomography. *Estuarine, Coastal and Shelf Science, 193*, 12-24.

Zhang, E., Savenije, H., Chen, S., & Mao, X. (2012). An analytical solution for tidal propagation in the Yangtze Estuary, China. *Hydrology & Earth System Sciences, 16*(9).

Zhu, X.-H., Zhu, Z.-N., Guo, X., Ma, Y.-L., Fan, X., Dong, M., et al. (2015). Measurement of tidal and residual currents and volume transport through the Qiongzhou Strait using coastal acoustic tomography. *Continental Shelf Research, 108*, 65-75.